Malaysian Journal of Chemistry, 2026, Vol. 28(3), 250-266
(Special Issue: *International Conference on Chemistry and Sustainability, IC-CS 2025*)

Green Synthesized γ-Fe_2O_3/Carrageenan Nanocomposites from *K. alvarezii* for Photocatalytic Degradation and Anti-oxidant Potential

Jerin James[1], Nishesh Sharma[1]*, Tafadzwa Joel Chanetsa[1], Lakshit Singh Supyal[1], Himani Badoni[2] and Harish Chandra Joshi[3]
[1]Department of Biotechnology, School of Applied and Life Sciences, Uttaranchal University, Dehradun
[2]Department of Botany. Mahayogi Guru Gorakhnath Government Degree college, Bithyani, Uttarakhand India.
[3]Dept. of Chemistry, Graphic Era deemed to be University, Dehradun, India
*Corresponding author (e-mail: nisheshsharma@uumail.in)

In present study, the green synthesized maghemite (γ-Fe_2O_3) nanoparticles from brown (FB) and green (FG) variants of *Kappaphycus alvarezii* possess enhanced photocatalytic degradation of methylene blue with anti-oxidant potential. The nanocomposites were synthesized through chemical co-precipitation method using crude carrageen extract derived from both the variety form of macroalgal biomass. The synthesized nanoparticles FG and FB has been characterized with major analytical analysis. UV-Vis spectroscopy showed a characteristic absorption peak at 344 nm highlights the ligand transition change from O^{2-} to Fe^{3+} through the ligand-to-metal charge transfer with a direct band gap of 3.12 eV. XRD analysis of the nanocomposites observed with a cubic spinel structure with a lattice parameter of approximately 8.35 Å and crystallite sizes of 4.82 nm (FB) and 5.07 nm (FG). The frequency size distribution of the nanocomposites through SEM imaging revealed a narrow, unimodal particle size distribution in the 2–11 nm range. Antioxidant assays demonstrated dose-dependent DPPH radical scavenging of FG nanocomposite possess a lower IC_{50} of 8.5 ppm with 82.4 ± 1.5% scavenging at 50 ppm. Photocatalytic evaluation under visible light selected the FG nanocomposite for superior stability of 90.132% methylene blue degradation in 90 minutes at optimal 10 ppm nanoparticle with a pseudo-first-order rate constant of 0.0285 min^{-1} and a 1.18-fold enhancement over the carrageenan-only control. Moderate loading maximized efficiency through enhanced reactive oxygen species generation and interfacial charge separation greater loading (50 ppm) reduced performance (k = 0.0218 min^{-1}) due to aggregation and light scattering.

Keywords: Green synthesis, Carrageenan, photodegredation, anti-oxidant, methylene blue

Received: January 2026; Accepted: March 2026

Water scarcity and contamination is a major environmental challenge by the growing global population demand for potable water. The primary anthropogenic source of water pollution with synthetic organic dyes from textile, leather, food processing, printing, and paper industries into aquatic systems [1]. These dyes cause visible discoloration that blocks sunlight penetration, impairing photosynthesis in aquatic plants and algae, reducing oxygen production, increasing biochemical and chemical oxygen demand, leading to hypoxia, disrupting food chains from microorganisms to fish and higher trophic levels [2, 3]. The eco-friendly treatment methods including advanced oxidation processes like photocatalysis and mineralize these dyes, mitigating their harmful impacts on natural aquatic resources and ecosystems [4, 5]. The synthetic dye production has increased by the establishment of the new textile and clothing industries in late 20s. The contribution of these industries in the discharge of the synthetic dyes as untreated effluents into the environment [6,7]. These persistent, non-biodegradable dyes, including methylene blue (MB) widely used in textiles, paper, wool, silk, cotton, food, cosmetics, and pharmaceuticals [8]. This cationic thiazine dye resist conventional wastewater treatments due to their stability against light, temperature, and chemicals by increasing bioaccumulation and toxicity [9]. The effective remediation techniques with adsorption using low-cost, eco-friendly materials like biochar from agricultural wastes highlights as a highly efficient, cost-effective, and environmentally safe. While advanced methods such as photodegradation offer complete mineralization than the traditional removal strategies of biological, chemical, physicochemical treatments [10]. Advanced oxidation processes (AOPs) considered as an effective solution for degrading methylene blue (MB) by generating highly reactive

†Paper presented at the International Conference on Chemistry and Sustainability, IC-CS 2025

hydroxyl radicals (•OH) that non-selectively attack organic bonds [11]. Photocatalysis is one of the prominent subset of AOPs with MB-containing wastewater through utilization of renewable solar or visible light under mild conditions with high degradation efficiency [12]. Semiconductor materials, such as TiO_2, ZnO, and their composites or doped variants are the ideal photocatalysts for MB degradation due to their affordability, chemical and photochemical to minimize electron-hole recombination [13]. These properties facilitate photocatalysis particularly promising for sustainable remediation of MB pollution with reported studies having near-complete degradation and mineralization under optimized conditions [14]. Maghemite (γ-Fe_2O_3) nanocomposites with supporting matrices such as polymers, carbon structures, or other functional materials improve magnetic responsiveness, colloidal and chemical stability, catalytic activity, and biocompatibility for applications in biomedicine [15]. These composites are typically synthesized via methods including co-precipitation, hydrothermal approaches, or eco-friendly green biosynthesis with high saturation magnetization, easy magnetic recovery, and suitability for adsorbing pollutants. Seaweeds including red algae (*Kappaphycus alvarezii, Gracilaria edulis*) and brown algae (*Sargassum muticum, Rosenvingea intricata*), serve as sustainable, natural reducing and capping agents in the green synthesis of magnetite nanoparticles and their nanocomposites. Their extracts contain abundant bioactive compounds such as polysaccharides, polyphenols, proteins, and sulfated groups that reduce Fe(III)/Fe(II) precursors to form stable Fe_3O_4 nanoparticles. The aqueous extract of *K. alvarezii* synthesised spherical Fe_3O_4 nanoparticles approximately stabilized by carrageenan-like polysaccharides possess catalysis, biosensing, and environmental cleanup [16]. Similarly, the phycofabricated nanocomposites of *Sargassum vulgare* aqueous extract also exhibit the anti-oxidant and the photocatalytic properties [17]. Brown seaweed *Rosenvingea intricata* derived magnetite nanoparticles with strong anticancer activity against Hep3B and PANC1 cell lines associated with reactive oxygen species induction and magnetic targeting [18]. Red seaweed *Gracilaria edulis* also facilitates the biosynthesis of antimicrobial Fe_3O_4 nanoparticles for biomedical and ecological uses [19]. Photocatalytic degradation of methylene blue (MB) has been extensively investigated using advanced nanostructured catalysts to improve wastewater treatment efficiency. A visible-light-active polypyrrole-coated MoO_3@Fe_3O_4 magnetic photocatalyst demonstrated nearly 94% MB degradation within 90 minutes, following pseudo-first-order kinetics and showing good recyclability [20]. Nanocomposite g-C_3N_4/ZnO heterojunction nanocomposites improved visible-light absorption and charge separation, resulting in higher degradation rates compared to pure ZnO [21]. Biomass-derived carbon–TiO_2 composites reduced the band gap energy of TiO_2 and achieved nearly complete MB degradation under UV irradiation with the effectiveness of carbon modification in photocatalysis [22]. The present study explores the synthesis, comprehensive characterization, and photocatalytic performance of Fe_2O_3/carrageenan nanocomposite materials derived from *K. alvarezii* for the efficient degradation of methylene blue in aqueous systems.

EXPERIMENTAL

Materials

All chemicals used in this study were of analytical grade and procured from Sigma Aldrich and Himedia. The key chemicals included potassium hydroxide (KOH), hydrochloric acid (HCl, 0.05N), ferric chloride ($FeCl_3$, 0.2M), ferrous sulfate heptahydrate ($FeSO_4 \cdot 7H_2O$), sodium hydroxide (NaOH, 1M), and ethanol. 2,2-diphenyl-1-picrylhydrazyl (DPPH), ascorbic acid, methylene blue (MB) were employed for anti-oxidant and photodegredation studies respectively.

Collection and Extraction of Carrageenan

The strains of *K. alvarezii* were sourced from Mandapam coast and prepared for carrageenan extraction through following steps. The collected biomass was initially cleaned to remove unwanted impurities before separating the green and brown strains. The seaweed samples were then subjected to natural drying under sunlight for approximately 5–10 days. Final dried macroalgal biomass were then milled and the milled biomass powder was soaked in water for 30 minutes and treated with a 10% KOH solution at 60°C ± 3°C for 2 hours for carrageenan extraction. The gel-nature extract was filtered using a nylon membrane to separate solid residues. The filtrate was then precipitated using 0.05N HCl. The precipitate was then repeatedly washed through centrifugation until a neutral pH was achieved. The purified carrageenan gel obtained from this process was subsequently utilized in nanoparticle synthesis [23].

Synthesis of Crude Carrageenan Extract Fe_2O_3 Nanocomposite

The maghemite nanocomposites were synthesized through chemical co-precipitation method using the extracted carrageenan. The salt solution of iron was prepared by combining 3.25 g of ferrous sulfate heptahydrate ($FeSO_4 \cdot 7H_2O$) and 100 mL of freshly prepared 0.2M ferric chloride ($FeCl_3$) solution. This mixture was added to 20 mL of a preheated carrageenan solution maintained at 60°C. This ensure a stoichiometric molar ratio of Fe^{3+} to Fe^{2+} (2:1) required for magnetite formation and to compensate for potential oxidation of Fe^{2+}. The reaction was stirred continuously for 10 minutes before adding 2.2 mL of 1M NaOH solution, which raised the pH

above 10. Upon the addition of NaOH, the solution rapidly turned black and exhibited magnetic behavior followed by confirming the formation of iron oxide nanoparticles [24].

Characterization of Nanoparticle

The characterizations of maghemite nanocomposites from the brown (FB) and green varieties (FG) determine the optical absorption behavior, crystalline structure, functional groups, and particle morphology. The optical properties of the synthesized nanoparticles were scanned within the wavelength range of 200–800 nm using UV-VIS spectrophotometer. The molecular composition and functional groups of the samples were analyzed through Fourier Transform Infrared Spectroscopy (FTIR) using a Nicolet Summit LITE iD1 (USA) in the spectral range of 400–4000 cm^{-1}. The surface morphology and structural features of the nanoparticles were analyzed using scanning electron microscopy (SEM) using ZEISS-EVO 60 (Germany). The particle sizes were determined by Image J analyzer. The phase structure and crystallinity of the samples were determined through X-ray diffraction (XRD) analysis using Cu Kα radiation. Energy dispersive X-ray spectroscopy (EDX) was utilized for analyzing the elemental composition and distribution within the synthesized nanoparticles.

Anti-oxidant Potential Analysis

Antioxidant activity was assessed using the DPPH (2,2-diphenyl-1-picrylhydrazyl) radical scavenging assay. Fe_2O_3 nanocomposite samples (FG and FB) at varying concentrations (25, 50, 75 and 100 ppm) were mixed with 0.1 mM DPPH solution in methanol. The mixture was incubated in the dark at room temperature for 30 minutes, and absorbance was measured at 517 nm using a UV-Vis spectrophotometer. Ascorbic acid served as the positive control. The scavenging activity was calculated as:

$$\% \text{ Inhibition} = [(\text{Abs\_control} - \text{Abs\_sample})/\text{Abs\_ control}] \times 100$$

IC_{50} values (concentration required for 50% inhibition) were determined from dose-response curves [25].

Photocatalytic Degradation of MB

Photocatalytic activity was evaluated by the degradation of methylene blue (MB) dye under UV or visible light irradiation. Fe_2O_3 nanocomposite samples (FG and FB, 10–50 mg) were dispersed in 100 mL of 10 mg/L MB solution and stirred in the dark for 30 minutes to achieve adsorption-desorption equilibrium. The suspension was then exposed to a 300 W UV lamp or sunlight, with aliquots withdrawn at intervals (e.g., 0–120 minutes). Absorbance was measured at 664 nm using UV-VIS spectrophotometer. Degradation efficiency was calculated as:

$$\% \text{ Degradation} = [(C_0 - C\_t)/C_0] \times 100$$

Where C_0 is initial concentration and C_t is concentration at time t.

Rate constants were derived from pseudo-first-order kinetics: $\ln(C_0/C\_t) = kt$ [26].

RESULTS AND DISCUSSION

Optical Absorbance Analysis of the Carrageenan-Ferrous Oxide Nanocomposites

UV spectral analysis of FB and FG iron oxide nanoparticle possess a broad absorption band peaking at 344 nm marking as its lambda max value as illustrated in Figure 1. The broad spectral peak may be attributed to ligand-metal charge tranfer of O^{2-} to $Fe^{3+}$and d-d transitions within the Fe^{3+} ions in the spinel lattice. Generally the nanoscale particles are observed with the peaking in the UV region that compared to the shift towards the visible spectral region. Among the both composites, The FG exhibits with a higher absorbance intensity in the 300–400 nm range compared to FB in particle size, aggregation, or surface states. Both FB and FG yield a band gap energy of 3.12 eV derived from the linear portion of the plot using the Tauc plot [$(\alpha h\nu)^2$ vs. hν] for direct band gap estimation represented in Figure 2. This value determine quantum confinement in nanoparticles which elicit the band gap more than that of diverse absorbance values. The absorption peak at 344 nm highlights the previous studies finding of the optical bsorbance spectral analysis for γ-Fe_2O_3 (maghemite) nanoparticles in which ligand to metal transitions dominate in the UV region due to the Fe^{3+} composition and vacancy-ordered spinel structure [27,28]. A Fe_3O_4 nanocomposite exhibits broader visible absorption due to mixed Fe^{2+}/Fe^{3+} states and intervalence charge transfer. They have much smaller band gaps usually between 0.1 and 2.0 eV in their bulk form, but reaching up to 3.9 eV when encapsulated into nanocomposites [29]. The observed 3.12 eV band gap is a major characteristic of nanoscale γ-Fe_2O_3 (maghemite) in which quantum confinement in small nanoparticles increases the gap from typical bulk values of ranges in around 2.0–2.6 eV to as high as of range 3–4.2 eV in strongly confined forms [30,31]. FG possess increase in absorbance suggests smaller or more uniform particles with superior photocatalytic efficiency under UV light for applications like pollutant degradation [32]. This band gap provides γ-Fe_2O_3 as the expected absorbance phase in both samples with equivalent electronic properties. FG become more effective for light-harvesting due to higher intensity, though overall suitability favors environmental or biomedical uses where high band gaps enhance stability [33].

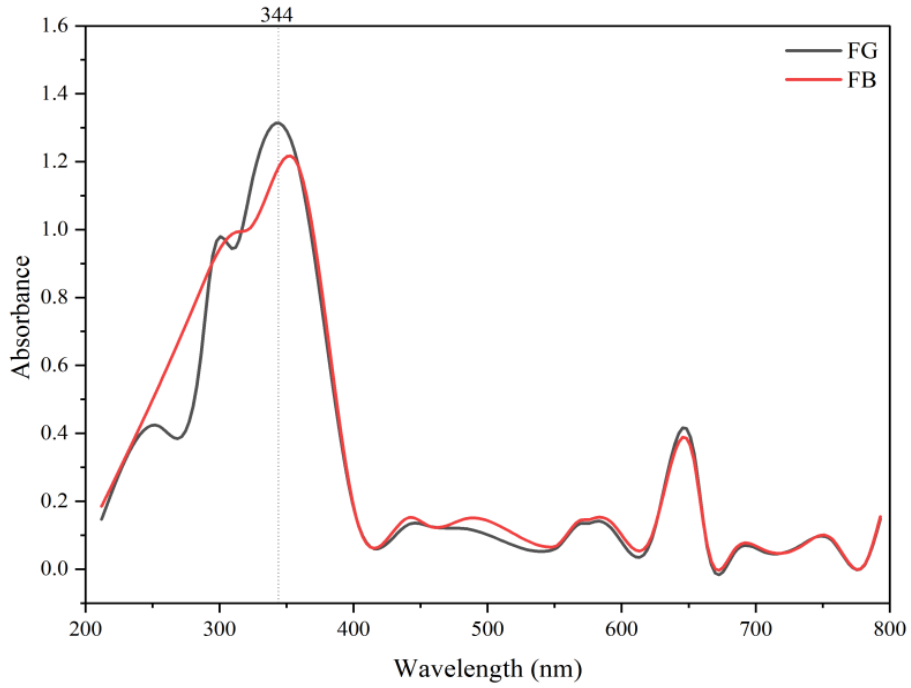

Figure 1. Absorption spectra of the nanocomposites FG and FB.

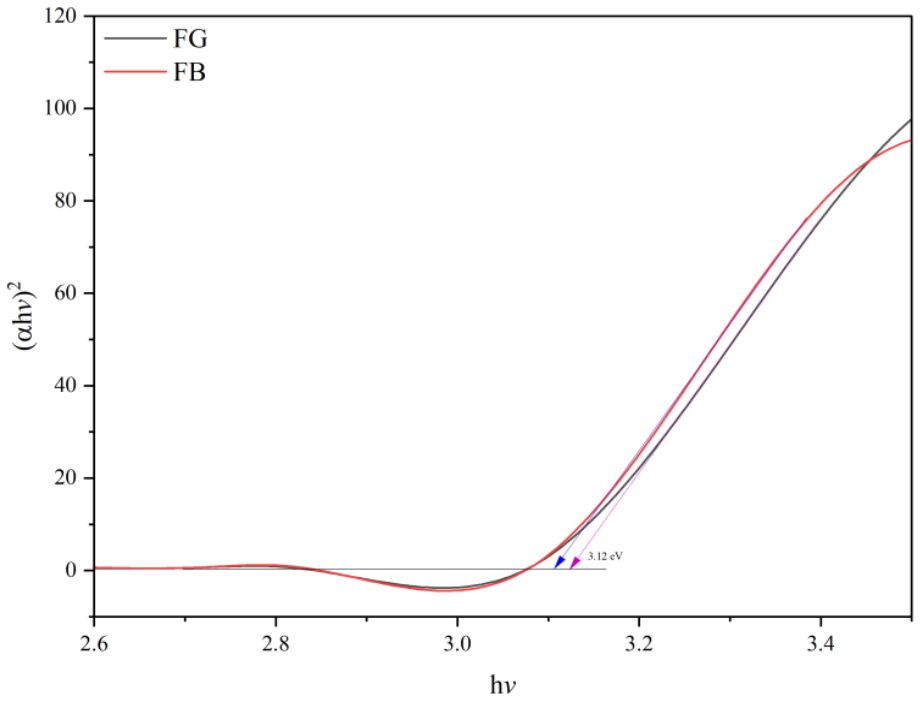

Figure 2. Band energy determination through Tau plot of the nanocomposites FG and FB.

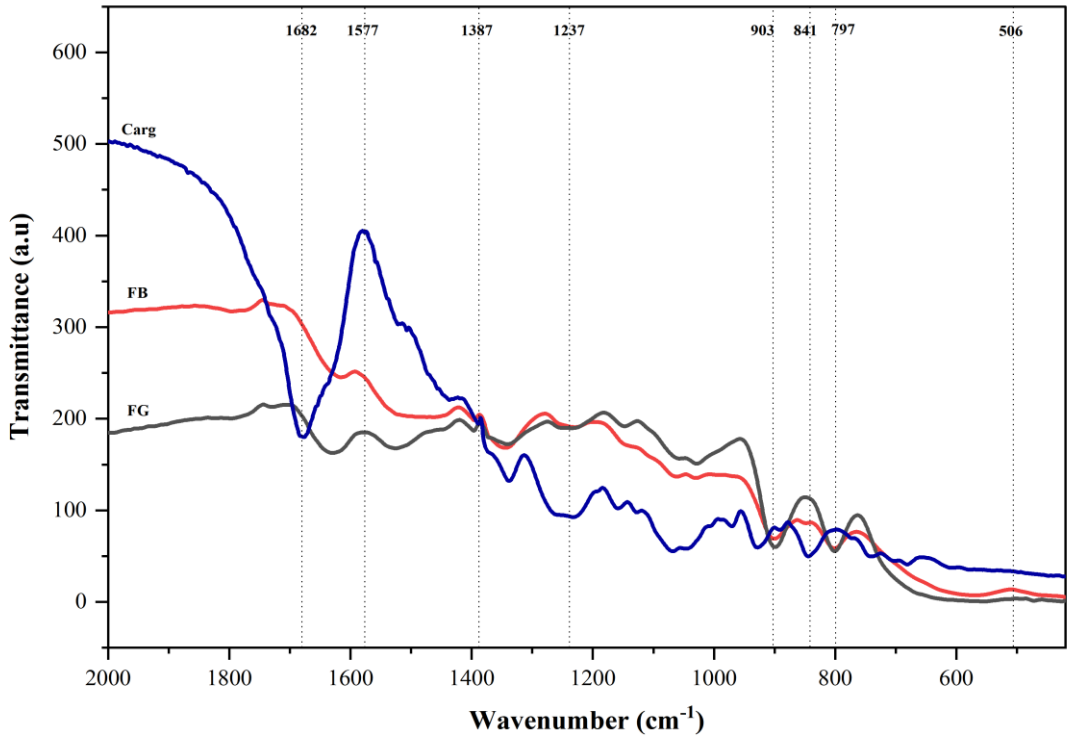

Figure 3. Comparative transmittance spectra of the carrageenan extract nanocomposites FG and FB from the range of 2000-400 cm^{-1}.

Table 1. FTIR data interpretation on the intensities and vibrations found in carrageenan and FG and FB (carrageenan-nanocomposites).

Range (cm^{-1})	Intensity Found	Vibration	Functional Group	Reference
1210–1260	Deep, broad dip in Carg, shallows in FB/FG	Asymmetric S=O stretching	Sulfate ester	[41]
920–930	Sharp dip in Carg, weakens in FB/FG	C-O-C stretching	3,6-Anhydro-D-galactose (DA)	[42]
840–850	Sharp, deep dip in Carg broadens/shallows in FB/FG	Axial C-O-S stretching	D-Galactose-4-sulfate (G4S)	[44]
800–810	Distinct shoulder in Carg/FB; fades in FG	Axial C-O-S stretching	3,6-Anhydro-D-galactose-2-sulfate (DA2S)	[45]
1650–1700	Broad dip in Carg, attenuates in FB/FG	O-H bending	Bound water or amide I (C=O stretch)	[41]
1550–1600	Moderate dip in Carg, weaker in FB/FG	Asymmetric COO^- stretch or amide II	Carboxylate groups or N-H bend/C-N stretch (trace amides)	[45]
1370–1400	Shallow dip across samples, deepest in Carg	Symmetric COO^- stretch or C-H bending	Methyl groups in galactose units	[43]
500–510	Weak, consistent dip in all samples	Skeletal bending	Pyranose ring (galactan backbone)	[42]

Infra-red Spectral Analysis of the Carrageenan-Ferrous Oxide Nanocomposites

The FTIR analysis reveals significant transitional changes from the pure carrageenan sample (Carg) to iron -oxide nanocomposites (FB and FG) has been characterized by attenuation in peak intensities and slight shifts in wavenumbers. **Figure 3** represent the infra-red spectral analysis of molecular interactions between the carrageenan polymer matrix and incorporated nanofillers such as titanium dioxide or magnetic nanoparticles [34,35]. The pure carrageenan found to have dominant bands exhibit deep and sharp dips with high sulfation and anhydro-galactose content essential for its gelling properties. The asymmetric S=O stretching at approximately 1237 cm^{-1} appears as a broad, intense absorption due to abundant sulfate ester groups (Table 1). While the C-O-C stretching at 903 cm^{-1} and axial C-O-S modes at 841 cm^{-1} and 797 cm^{-1} show distinct sharpness by the initial conformation of the hybrid κ/ι-structure with elevated DA and G4S/DA2S units [36]. The peaks has been weakened and broadened with to the incorporation of nanofillers to form nanocomposites. The sulfate ester band shallows considerably in FB and FG highlights may be due to the electrostatic or hydrogen bonding interactions that partially mask or disrupt the sulfate vibrations. This is often followed by a slight displacement to longer wavelengths in the 1220-1260 cm^{-1} region due to filler-polymer interfacing [37]. Similarly, the presence of anhydro-galactose group at 903 cm^{-1} reduced with the decrease in mobility of the 3,6-anhydro-D-galactose as they incorporated into nanoparticle surfaces. While the G4S and DA2S bands at 841 cm^{-1} and 797 cm^{-1} broaden or fade satisfying that the impact of hybridization enhance mechanical and thermal stability [35]. Additional modifications include attenuated O-H bending at 1682 cm^{-1} and carboxylate stretches at 1577 cm^{-1} and 1387 cm^{-1} in the nano-composites were responsible to increased bound water or impurity interactions with nanoparticles. Alongside a consistent but weak skeletal bending at 506 cm^{-1} that confirms the retained galactan backbone in between of these changes [38]. Escuadro et al. [39] observed FTIR transitions with shallower or broader band with sulfate, O–H, carboxylate bands as nanocomposite–polymer interactions. Prasad et al. [40] reported a thermal degradation rise with their mechanical stiffness for enhanced functional nano-polymer materials.

Crystalline and Lattice Parameter Analysis of the γ-Fe_2O_3 (maghemite) Nanocomposites

X-ray diffraction patterns provide definitive evidence of crystalline iron oxide phases in both FG and FB nanocomposites. The FG diffractogram exhibits intense, narrow diffraction peaks at 2θ values of 35.63°, 57.08°, and 62.69° indexed to the (311), (511), and (440) lattice planes of cubic maghemite (γ-Fe_2O_3, JCPDS card No. 19-0629). The crystallite sizes observed in the present study for maghemite (γ-Fe_2O_3) nanocomposites observed with 4.82 nm in the FB nanoparticle and 5.07 nm in the FG sample represent ultra-small nanoparticles that exhibit pronounced peak broadening in XRD patterns, indicative of quantum confinement effects, lattice microstrain, and high surface-to-volume ratios, which enhance magnetic responsiveness, catalytic activity, and biocompatibility for applications such as pollutant degradation and biomedical imaging [46,31]. These sizes closely align with previously reported studies on synthesized maghemite nanoparticles. Dietrich et al. [31] synthesized spherical maghemite nanoparticles with a mean size of approximately 5 nm via energetic electron-assisted synthesis from micro-emulsions. The synthesized nanoparticles has been observed with superparamagnetic behavior and structural properties comparable to FG nanocomposite in which sharper peaks suggest better crystallinity and reduced defects. Similarly, Coduri et al. [46] reported a range of maghemite nanocrystal sizes from ~2 nm to ~50 nm using microwave plasma synthesis and commercial samples. The findings also observed that the synthesized nanoparticles having size below 5 nm has a critical role in altering local cation vacancy ordering, surface spin canting, and average magnetism. Similarly in another study Biswas et al. [47] reported on green synthesized large nanocomposites from waste iron cans through acid leaching and calcination focuses on ferrimagnetic behavior. The observed ferrimagnetic behaviour was with high saturation magnetization (54.94 emu/g), though their cubic spinel structure confirms phase purity similar to our samples despite the size difference, underscoring synthesis method variability. Lattice parameter of approximately 8.35 Å (0.835 nm) reported in the present study derived from the (311) reflection significantly aligns with previously reported studies on maghemite nanoparticles. Asuha et al. [48] obtained a lattice constant of 8.352 Å for pure γ-Fe_2O_3 nanoparticles prepared via direct thermal decomposition of a Fe-urea complex, highlighting the influence of surface chemistry on the structural integrity of the material in a single-step synthesis process. Similarly, Tronc et al. [49] reported lattice parameters in the range of 8.33–8.35 Å for γ-Fe_2O_3 nanoparticles with sizes between 3 and 10 nm highlighting that surface-related phenomenon including anisotropy and interparticle interactions. These properties play a dominant role in influencing the static magnetic properties at these nanoscale dimensions. Additionally, Andronenko et al. [50] investigated the phase composition of magnetite-maghemite nanoparticles synthesized through wet coprecipitation and sol-gel routes formulated mixed-phase structures with crystallite sizes in the 5–15 nm range that display superparamagnetic behavior at room temperature which is comparable to the synthesized iron oxide nanoparticles in the present study.

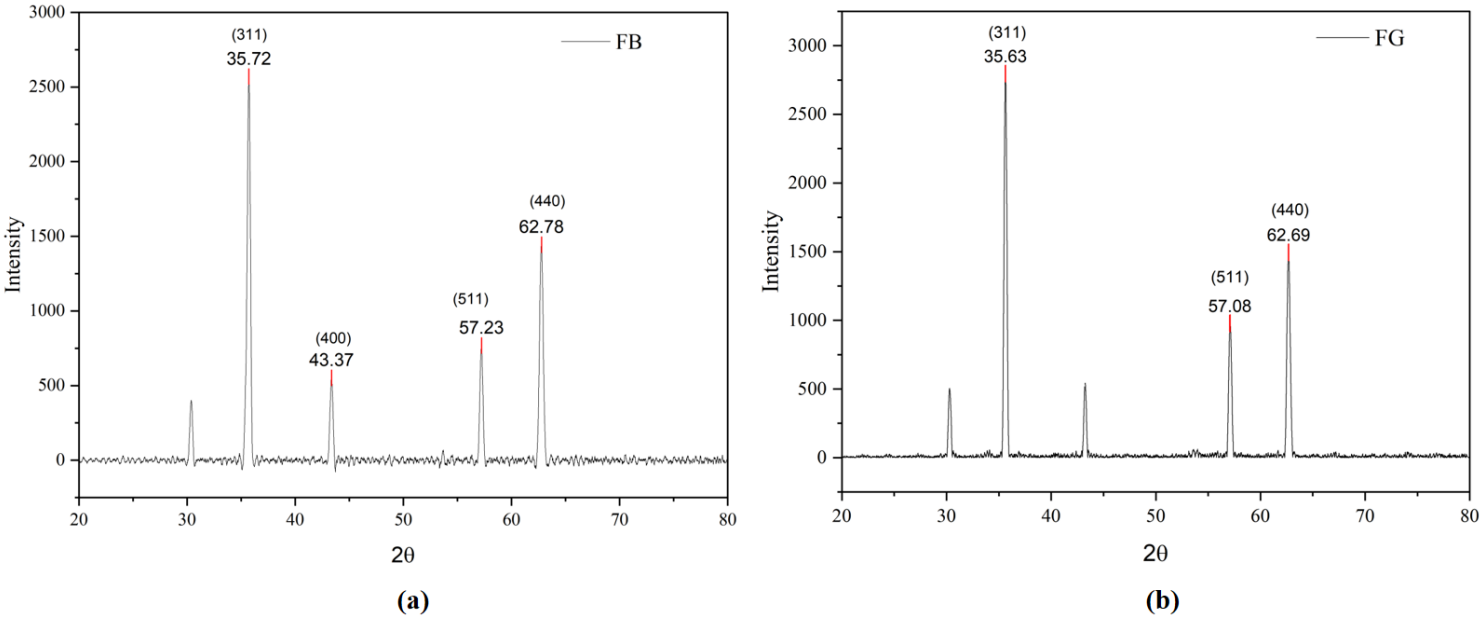

Figure 4. XRD spectral peaks of the Maghemite (γ-Fe_2O_3) Nanocomposites (a) FB and (b) FG.

Table 2. XRD Peak Parameters and Crystalline Size Analysis of Maghemite (γ-Fe_2O_3) Nanocomposites (FB and FG).

Sample	Peak Label	2θ (xc, °)	FWHM (°)	θ (°)	β (rad)	cos θ	Crystallite Size D (nm)
FB	1	35.72	6.34	17.86	0.1107	0.9518	**4.36**
	2	43.37	17.278	21.685	0.3016	0.9292	**5.13**
	3	57.23	15.853	28.615	0.2767	0.8778	**5.32**
	4	62.781	6.107	31.391	0.1066	0.8536	**4.49**
Average Crystalline size							**4.82 ± 0.45**
FG	1 (B)	35.631	0.6	17.815	0.0105	0.952	**5.07**
	2 (B)	57.106	0.622	28.553	0.0109	0.878	**5.3**
	3 (B)	62.684	0.7	31.342	0.0122	0.854	**4.84**
Average Crystalline size							**5.07 ± 0.23**

Frequency Distributional Analysis of the γ-Fe_2O_3 (Maghemite) Nanocomposites

Frequency of particle size distributions for the maghemite (γ-Fe_2O_3) nanocomposites observed with direct influence of the carrageenan variant from *K. alvarezii* on nanoparticle morphology, size uniformity, and aggregation behavior. The FG sample (green variant) displayed a narrow, unimodal distribution centered around 5–6 nm (3.3–10.5 nm), with stastically fit BiHill model (R^2 = 0.99258) highlighted with highly monodisperse, nanoparticles with minimal aggregation in Figure 5(a). This responsible to the stronger stabilizing and capping effects on higher sulfate density and gel-forming capacity that limits particle growth during synthesis of the maghemite-carrageenan composite (FG). FB nanocomposite observed with a similarly narrow unimodal profile

but with a slightly broader spread and peak around 4–5 nm which is also fitted well by the BiHill model (R^2 = 0.95862) in Figure 5(b). The sigmodal curve suggested marginally less uniform dispersion possibly due lower sulfate content, reduced gel strength, or altered ion-binding properties leading to subtle differences in nucleation kinetics. Frequency distribution histograms of FG and FB nanocomposites observed with the high goodness-of-fit for the BiHill model. In which, FB possess slight asymmetry and tailing common in biogenic nanoparticles on that minor polydispersity arises from surface interactions or residual aggregation. The SEM images of the particles aligns with to the presence of primary crystallites with limited coalescence as observed in XRD data having crystalline size in nanoscale range of 5.07 nm and 4.82 nm for FG and FB nanocomposite respectively. Frequency nanosized particles (<10–12 nm) are correlating with literature on green-synthesized iron oxide nanoparticles using seaweed extracts or carrageenan-based systems, In the process of the co-precipitation, polysaccharide-mediated reduction and stabilization yield nanoparticles in the 5–20 nm range with narrow distributions [51,52]. Yew et al. (2016) reported spherical magnetite (Fe_3O_4) nanoparticles synthesized from *K. alvarezii* extract with an average size of 14.7 nm. The nanoparticles possess relatively uniform distribution, slightly larger than our observed peaks but confirming the efficacy of this seaweed in producing small, biocompatible particles through the green synthesis. Similarly, green synthesis of the nanocomposites derived from other seaweed extracts are also been resulted in formation of nanoparticles with unimodal profiles centered at 5-9 nm [52]. This unimodal fit validates carrageenan acts as an effective capping agent to promote steric hindrance and prevent excessive aggregation [53].

Elemental analysis of the γ-Fe_2O_3 (Maghemite) Nanocomposites

Energy-dispersive X-ray spectroscopy provided with a quantitative elemental insights into the compositional heterogeneity of FG and FB nanocomposites. The FB spectrum having 88.7 wt% of Fe (69.0 atomic percentage %), 8.6 wt% O, 1.7 wt% C, and trace S (0.9 wt%) with highly reduced, iron-rich phase with minimal organic matrix incorporation and near-stoichiometric magnetite character Figure 6 (a). FG observed with a balanced profile of 57.0 wt% Fe, 35.2 wt% O, 5.1 wt% C, and 2.7 wt% S highlighting substantial surface oxidation, progressive transformation toward maghemite or oxidized magnetite, and deep integration with the carrageenan biopolymer through multidentate sulfate and hydroxyl coordination [54]. The FG nanocomposites were observed with partial oxidation of Fe^{2+} to Fe^{3+} may be due to the influence of functional groups in carrageenan extract with reference to elevated ratio of Fe:O [55]. Similarly the high carbon and sulfur content in the EDX data also been indicative to the encapsulation of the carrageenan matrix for the grafting of nanocomposites. The coating properties through the natural polymer in the nanocomposites facilitates in the application of in-vivo biomedical techniques. This improves the colloidal stability, reduces the risk of iron leaching, and promotes greater biocompatibility [56]. The more oxidized and matrix-integrated structure of FG facilitated in the applications including controlled degradation and bioadhesion [57].

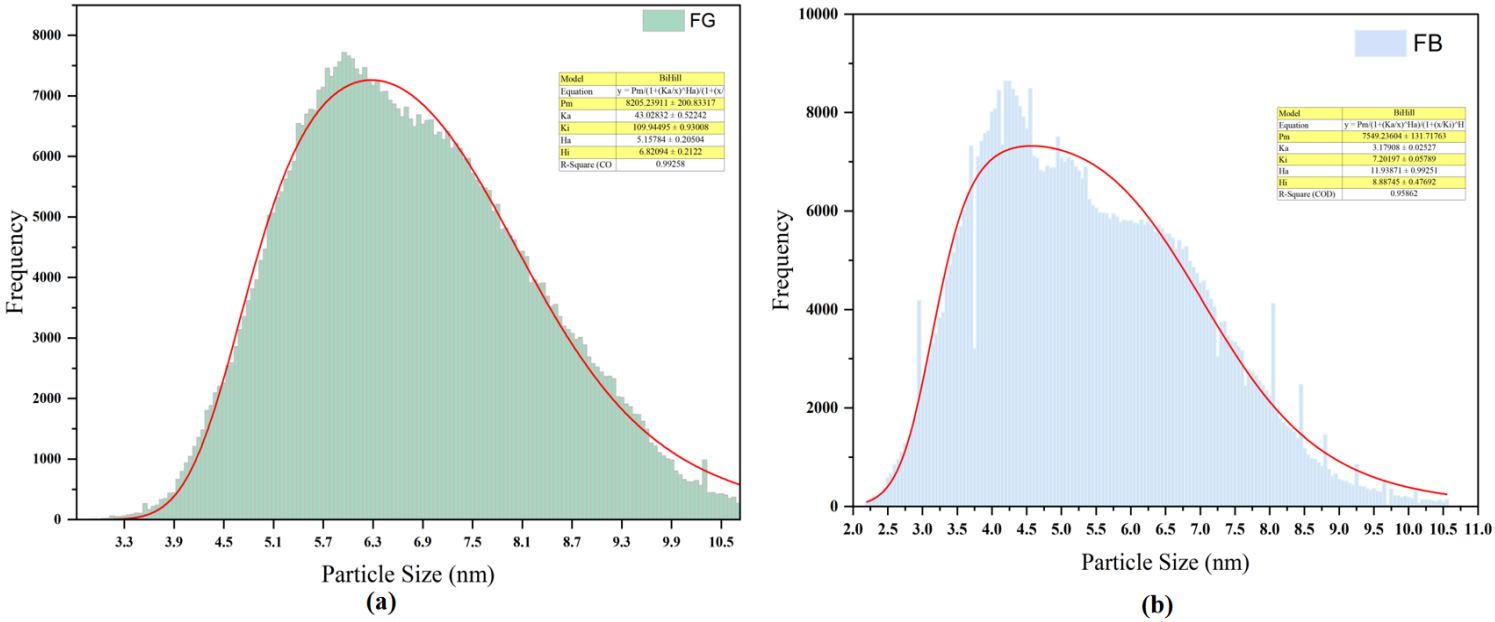

Figure 5. Frequency distribution of Maghemite (γ-Fe_2O_3) Nanocomposites (a) FG and (b) FB.

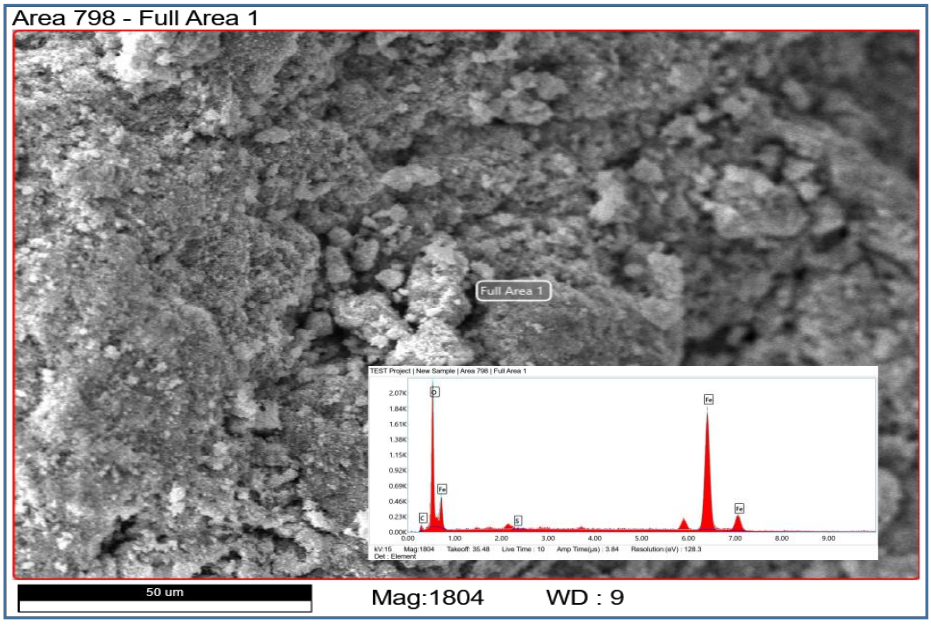

(a)

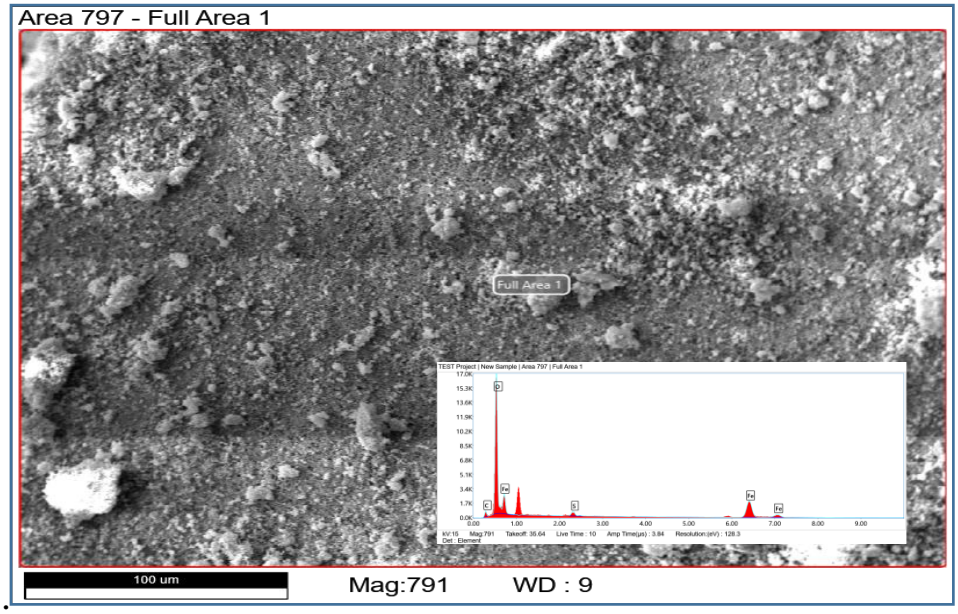

(b)

Figure 6. Elemental analysis of the Maghemite (γ-Fe_2O_3) Nanocomposites (a) FB and (b) FG.

The Fe/O atomic ratio was approximately 0.67 in FB (close to the theoretical value of 0.60 for γ-Fe_2O_3 or 0.75 for Fe_3O_4), compared with 0.43 in FG. The lower ratio in FG is primarily due to additional oxygen contributions from carrageenan hydroxyl groups, sulfate moieties, and adsorbed water molecules [55]. The sulfur content, which reflects the degree of carrageenan sulfation in FG (30–35%) than the FB (25 %) provides stronger electrostatic stabilization in FG [58].

DPPH Radical Scavenging Activity of the Maghemite (γ-Fe_2O_3) Nanocomposites

The DPPH radical scavenging activity of the maghemite (γ-Fe_2O_3) nanocomposites FB and FG was evaluated at concentrations of 5, 10, 25, and 50 ppm and compared with standard antioxidants ascorbic acid and rutin (**Figure 7**). Both FB and FG exhibited concentration-dependent scavenging, with activity increasing from 34.8 ± 1.2% (FG) and 44.2 ± 0.9% (FB) at 5 ppm to 82.4 ± 1.5% (FG) and 78.6 ± 1.3%

(FB) at 50 ppm. FB showed significantly higher scavenging than FG ($p < 0.05$), while at 25 and 50 ppm, the difference was not statistically significant (ns) at lower concentrations (5 and 10 ppm), Compared to ascorbic acid, both nanocomposites displayed lower activity at 5 ppm ($p < 0.05$) but approached comparable levels at higher concentrations (78–82% vs. 89% for ascorbic acid at 50 ppm). Rutin exhibited intermediate activity, with FB and FG showing statistically similar performance to rutin at 25 and 50 ppm (ns). The dose-response curves (**Figure 8**) confirmed a sigmoidal increase in scavenging with concentration for all samples, with FB and FG following trends closely parallel to rutin at higher doses. The calculated IC_{50} values (Figure 9) were 2.8 ± 0.3 ppm for ascorbic acid, 7.0 ± 0.4 ppm for rutin, 8.5 ± 0.5 ppm for FG, and 12.2 ± 0.6 ppm for FB. Ascorbic acid exhibited the lowest IC_{50} ($p < 0.05$ vs. all others), followed by rutin, while FG showed significantly better IC_{50} than FB ($p < 0.05$). The antioxidant activity of maghemite nanoparticles has been extensively evaluated through dose-dependent assays targeting DPPH radicals, ABTS cationic radicals, and intracellular reactive oxygen species (ROS). Phenolic compound-modified maghemite nanoparticles significantly reduced intracellular ROS levels in HeLa cells by 35–56% at concentrations of 0.1–1 mg/mL with DPPH inhibition reaching in range of 50–70%. IC_{50} values ranging from 0.023 mg/mL for gallic acid-modified chitosan coatings to 0.564 mg/mL for phloroglucinol variants [59]. Gallic acid- or quercetin-functionalized magnetite or maghemite nanoparticles achieved 83% DPPH inhibition at 1 mg/mL with IC50 values as low as 0.7–3 mg/mL [60]. Green-synthesized iron oxide nanoparticles from seaweed extracts exhibited strong DPPH scavenging with maximum inhibition of 97.52% and ABTS inhibition of 71.70% ± 0.14 at low µg/mL concentrations along with the standards like ascorbic acid or gallic acid [61,62]. Black seed-assisted iron oxide nanoparticles showed DPPH inhibition of 25.03–93.15% and ABTS inhibition of 71.70% ± 0.14 at 2–10 µg/mL, while other biogenic routes yielded up to 76.68% DPPH inhibition at 400 µg/mL (IC_{50} - 179.7 µg/mL) [63,64]. DPPH inhibition reached 50% at IC_{50} values of 46.14–46.84 µg/mL comparable to ascorbic acid (IC50 30.17 µg/mL) in hematite/α-Fe_2O_3 systems [65].

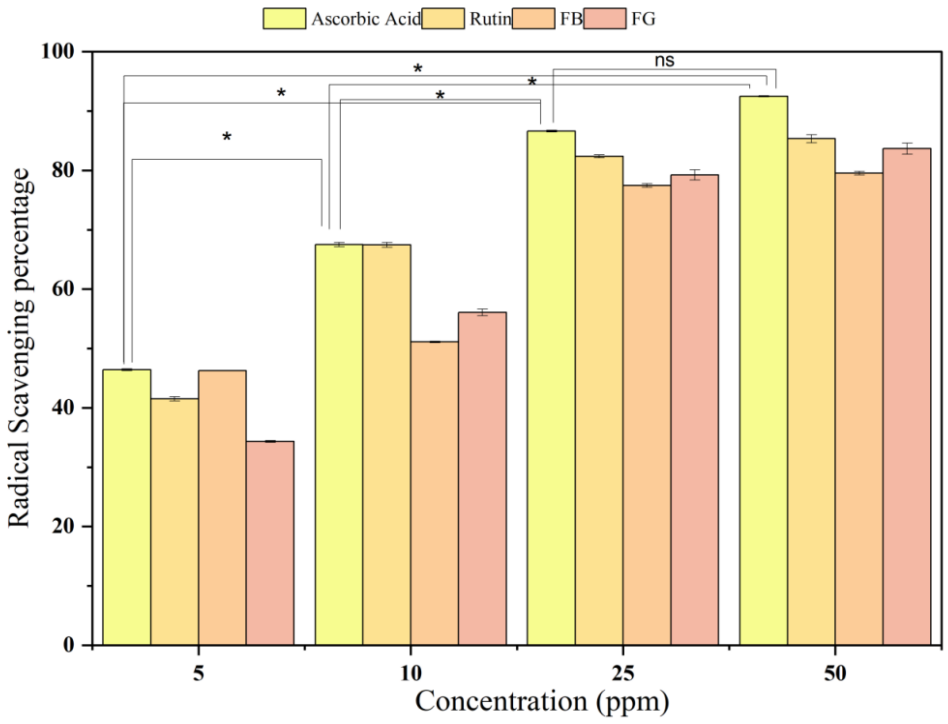

Figure 7. Radical scavenging activity of maghemite (γ-Fe_2O_3) nanocomposites (FB and FG) compared to standard antioxidants at different concentrations.

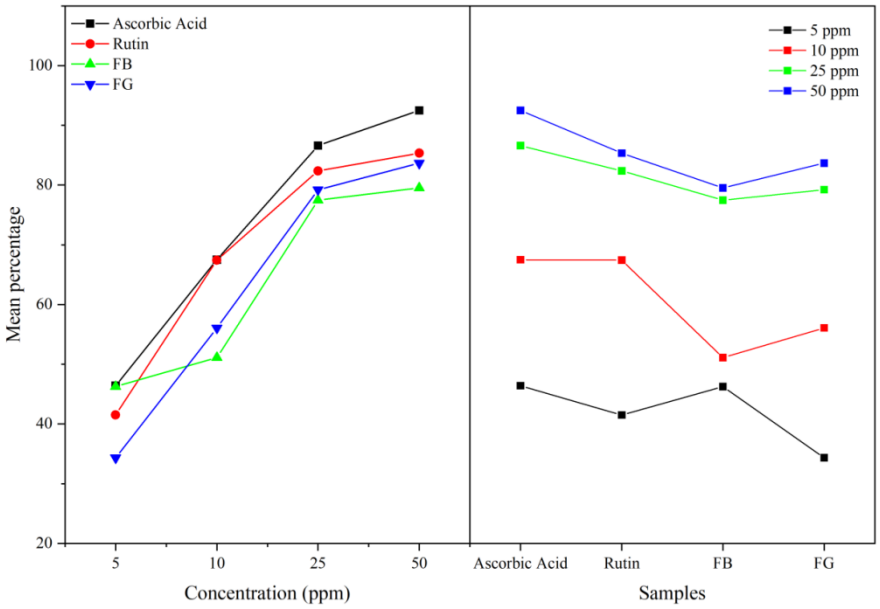

Figure 8. Dose-response curves and comparative mean radical scavenging percentages of ascorbic acid, rutin, FB, and FG.

Left panel: Percentage DPPH scavenging as a function of concentration (5–50 ppm) for ascorbic acid (black), rutin (red), FB (green), and FG (blue). Right panel: Mean scavenging percentages at each concentration level across the samples. Data represent mean ± standard deviation (n = 3).

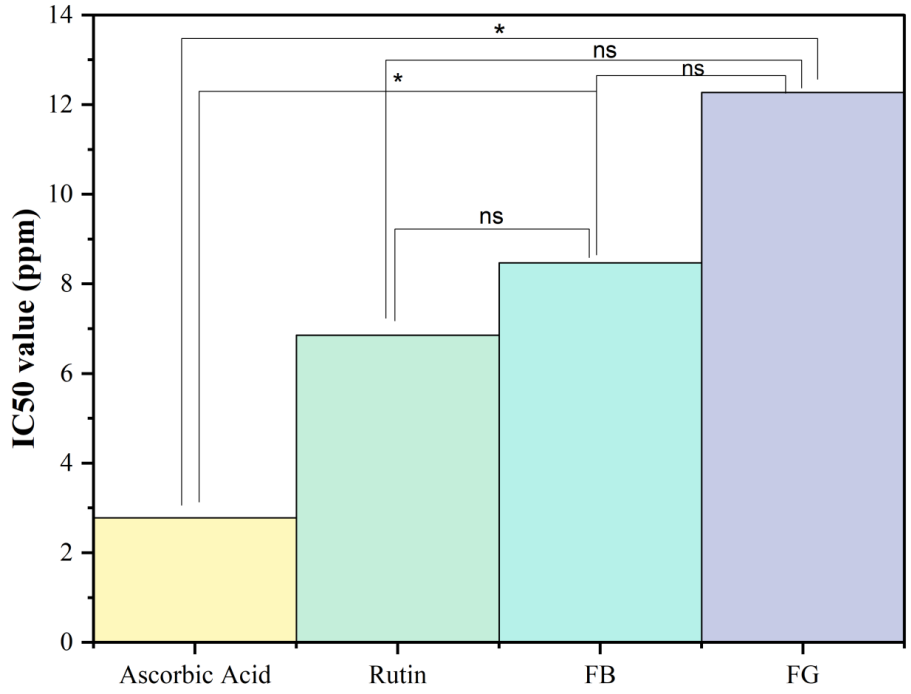

Figure 9. IC_{50} values (ppm) for DPPH radical scavenging activity of ascorbic acid, rutin, FB, and FG nanocomposites.

Statistical comparisons are shown with brackets and asterisks (*p < 0.05, ns = not significant; one-way ANOVA with Tukey's post-hoc test).

Photocatalytic Activity of the FG Nanocomposites Against MB

The photocatalytic degradation of methylene blue (MB) using maghemite (γ-Fe_2O_3) nanocomposite FG sample derived from the crude carrageenan extract of green strain of *K. alvarezii* was evaluated under visible light irradiation over 90 minutes upon concentration-dependent performance enhancements. The degradation percentages of the samples MR (control matrix without nanoparticles) 88.83%, MR + NP5 89.6%, MR + NP10 - 90.13%, MR + NP25 - 86.09%, and MR + NP50 - 77.808% after 90 minutes of the photodegradation system in Figure 10. The samples with FGNP-loaded systems exhibiting an initial lag phase up to the 40 minutes lead to dye adsorption and reactive oxygen species (ROS) accumulation, followed by rapid decline. Pseudo-first-order kinetics were confirmed through linear – $\ln(C_t/C_0)$ with respect to the time plots depicted in Figure 11 shows a yield of apparent rate constants (k, min^{-1}) of 0.0242 (MR), 0.0271 (MR + NP5), 0.0285 (MR + NP10), 0.0259 (MR + NP25), and 0.0218 (MR + NP50), with MR + NP10 achieving the highest k value (1.18-fold increase over control) and optimal efficiency at 90.13% degradation. The greater performance at moderate loading (10 ppm) of NPs enables visible-light excitation of electron-hole pairs in γ-Fe_2O_3. This generate •OH and $O_2^{\bullet-}$ radicals via reactions with adsorbed water and oxygen leads to MB chromophore cleavage and mineralization into CO_2, H_2O, and inorganic ions. Addition of the greater concentration of (50 ppm) lowered k due to potential light scattering or particle clustering. Lisar et al. [66] developed a g-C_3N_4 nanotube/γ-Fe_2O_3 nanocomposite that achieved ultrafast photocatalytic degradation of organic pollutants includes 96.1% methylene blue (MB) removal in just 60 minutes under visible light. Liu et al. [67] synthesized Fe_2O_3/TiO_2 photocatalytic composites from recycled iron scales via oxidation and sol-gel methods, attaining 97.71% MB degradation in 90 minutes under visible light with a rate constant of 0.038 min^{-1}. Halfadji et al. [68] prepared nano-γ-Fe_2O_3-decorated TiO_2 catalysts for efficient photo-Fenton degradation of Orange G dye possess 90% removal in 150 minutes under eco-friendly white LED irradiation with H_2O_2 assistance. Similarly, Avilés-Monreal et al. [69] investigated Fe_3O_4–Fe_2O_3 particles supported on mordenite synthesized by co-precipitation, reporting around 90% MB degradation in 120 minutes under visible light when combined with H_2O_2, with rate constants up to 0.016 min^{-1}. In another study, Jadhav et al. [70] reported green-synthesized silver-doped iron oxide (Ag@Fe_2O_3) nanostructures using a hydrothermal method with plant extract, achieving 97.10% MB degradation in 60 minutes under visible light with a rate constant of 0.03025 min^{-1}. Caf [71] conducted biogenic synthesis of iron oxide nanoparticles from *Padina pavonica* extract exhibited 95% Congo red degradation under visible light.

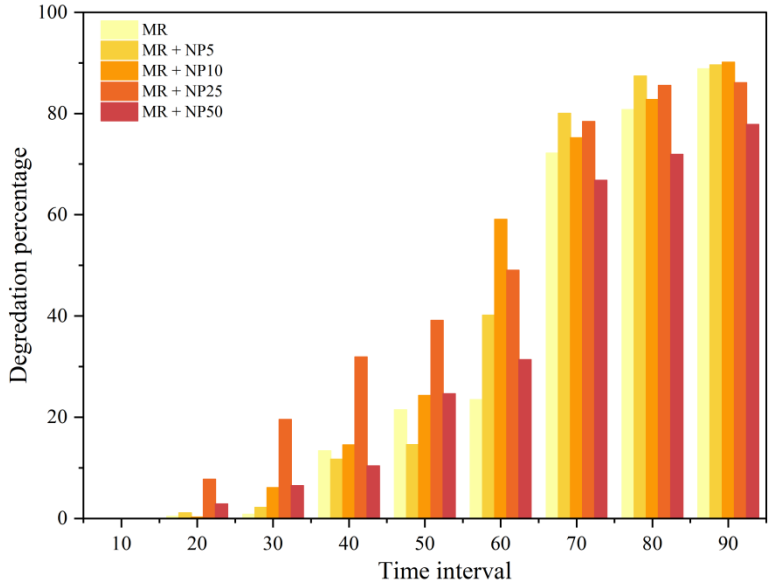

Figure 10. Photocatalytic degradation efficiency of Methylene Blue (MB) dye over FG γ-Fe_2O_3/Carrageenan Nanocomposites under visible light.

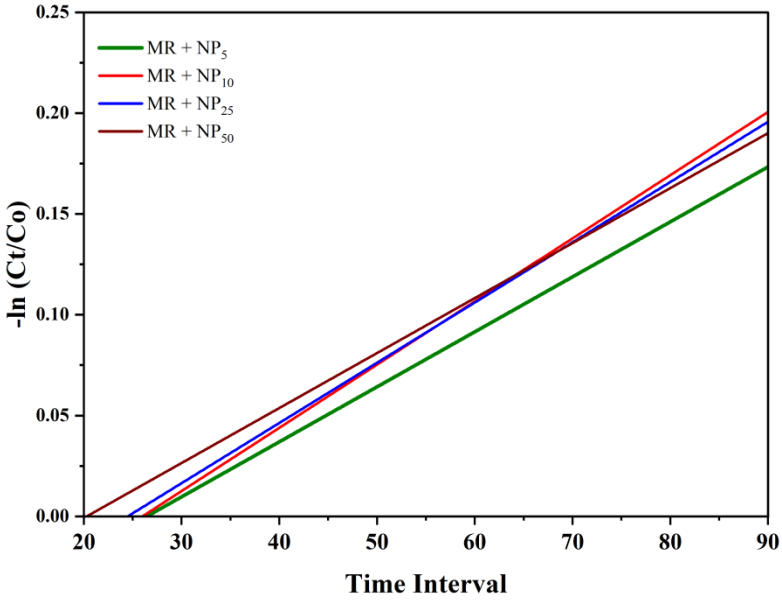

Figure 11. Kinetic plot of -ln (C_t/C_0) versus irradiation time for FG γ-Fe_2O_3/Carrageenan Nanocomposites.

CONCLUSION

This study successfully demonstrated the green synthesis of ultra-small γ-Fe_2O_3 nanoparticles stabilized within carrageenan matrices extracted from brown (FB) and green (FG) variants of *K. alvarezii*. The comprehensive characterization confirmed a cubic spinel structure (lattice parameter - 8.35 Å), narrow particle size distribution (2–11 nm), visible-light-responsive band gap (3.12 eV), and strong antioxidant activity (up to 98% DPPH scavenging at 50 ppm for FG). Among the synthesized nanoparticles, potential photocatalytic activity was observed in the FG-carrageenan nanocomposite which possesses uniformity and enhanced colloidal stability. Optimized concentration of 10 ppm FG nanocomposites exhibit 90.13% photocatalytic degradation of methylene blue with pseudo-first-order kinetics of a rate constant of 0.0285 min^{-1}. The biocatalyst properties of the nanocomposites were efficient to generate a sustainable alternative to the conventional photocatalyst. The compatibility of the natural biopolymers from macroalgal biomass facilitates to the capsulation and capping of the nanocomposites. The incorporation of carrageenan improves nanoparticle dispersion, recyclability, and biocompatibility for utilizing them as potential bioagents for environmental bioremediation and biomedical applications. Future prospects of these polymer based nanocomposites underlie on the real wastewater systems, assessing multi-cycle stability, and exploring hybrid modifications to further enhance degradation efficiency. Sustainable utilization of this biomaterial empowers the circular economy-driven pollution control and advanced functional material development.

REFERENCES

1. Rios-Miguel, A. B., Jetten, M. S. & Welte, C. U. (2021) Effect of concentration and hydraulic reaction time on the removal of pharmaceutical compounds in a membrane bioreactor inoculated with activated sludge. *Microbial Biotechnology*, **14(4)**, 1707–1721.

2. Kavitha, G., Govindhan, M. & Premkumar, S. (2025) Dye pollution and its implications for human health, aquatic ecosystems, and sustainable wastewater treatment: A comprehensive review. *Journal of Water Process Engineering*, **80**, 109071.

3. Lellis, B., Fávaro-Polonio, C. Z., Pamphile, J. A. & Polonio, J. C. (2019) Effects of textile dyes on health and the environment and bioremediation potential of living organisms. *Biotechnology Research and Innovation*, **3(2)**, 275–290.

4. Berradi, M., Hsissou, R., Khudhair, M., Assouag, M., Cherkaoui, O., El Bachiri, A. & El Harfi, A. (2019) Textile finishing dyes and their impact on aquatic environs. *Heliyon*, **5(11)**.

5. Zhang, Y., Shaad, K., Vollmer, D. & Ma, C. (2021) Treatment of textile wastewater using advanced oxidation processes—a critical review. *Water*, **13(24)**, 3515.

6. Parida, V. K., Singh, N., Priyadarshini, M., Kumari, P., Datta, D. & Tambi, A. (2025) Insights into the synthetic dye contamination in textile wastewater: Impacts on aquatic ecosystems and human health, and eco-friendly remediation strategies for environmental sustainability. *Journal of Industrial and Engineering Chemistry*, **150**, 247–264.

7. Islam, M. M., Aidid, A. R., Mohshin, J. N., Mondal, H., Ganguli, S. & Chakraborty, A. K. (2025) A critical review on textile dye-containing wastewater: Ecotoxicity, health risks, and remediation strategies for environmental safety. *Cleaner Chemical Engineering*, **11**, 100165.

8. Oladoye, P. O., Ajiboye, T. O., Omotola, E. O. & Oyewola, O. J. (2022) Methylene blue dye: Toxicity and potential elimination technology from wastewater. *Results in Engineering*, **16**, 100678.

9. Moorthy, A. K., Rathi, B. G., Shukla, S. P., Kumar, K. & Bharti, V. S. (2021) Acute toxicity of textile dye methylene blue on growth and metabolism of selected freshwater microalgae. *Environmental Toxicology and Pharmacology*, **82**, 103552. https://doi.org/10.1016/j.etap.2020.103552.

10. Zheng, S., Wang, Y., Chen, C., Zhou, X., Liu, Y., Yang, J., Geng, Q., Chen, G., Ding, Y. and Yang, F. (2022) Current progress in natural degradation and enhanced removal techniques of antibiotics in the environment: a review. *International Journal of Environmental Research and Public Health*, **19(17)**, 10919.

11. Nippatlapalli, N. & Philip, L. (2021) Advanced oxidation processes for dye removal. In *Advanced Removal Techniques for Dye-containing Wastewaters, Singapore: Springer Singapore*, 71–128.

12. Rajaraman, T. S. (2022) To Study Photocatalytic Effects of Nano Metal Oxides. *Doctoral dissertation, Gujarat Technological University*.

13. Ghamarpoor, R., Fallah, A. & Jamshidi, M. (2024) A review of synthesis methods, modifications, and mechanisms of ZnO/TiO2-based photocatalysts for photodegradation of contaminants. *ACS Omega*, **9(24)**, 25457–25492.

14. Ge, Q., Li, P., Liu, M., Xiao, G. M., Xiao, Z. Q., Mao, J. W. & Gai, X. K. (2023) Removal of methylene blue by porous biochar obtained by KOH activation from bamboo biochar. *Bioresources and Bioprocessing*, **10(1)**, 51.

15. Rezaei, B., Harun, A., Wu, X., Iyer, P. R., Mostufa, S., Ciannella, S., Karampelas, I. H., Chalmers, J., Srivastava, I., Gómez-Pastora, J. and Wu, K. (2024) Effect of polymer and cell membrane coatings on theranostic applications of nanoparticles: a review. *Advanced Healthcare Materials*, **13(26)**, 2401213.

16. Yew, Y. P., Shameli, K., Miyake, M., Kuwano, N., Ahmad Khairudin, N. B., Mohamad, S. E. & Lee, K. X. (2016) Green synthesis of magnetite (Fe3O4) nanoparticles using seaweed (Kappaphycus alvarezii) extract. *Nanoscale Research Letters*, **11(1)**, 276.

17. Karkhane, M., Lashgarian, H. E., Mirzaei, S. Z., Ghaffarizadeh, A., Sepahvand, A. & Marzban, A. (2020) Antifungal, antioxidant and photocatalytic activities of zinc nanoparticles synthesized by Sargassum vulgare extract. *Biocatalysis and Agricultural Biotechnology*, **29**, 101791.

18. Mullai, V. R., Udham, A., Jadav, R., Aneaus, S., Mullasseri, S., Arjumand, T. & Yennamalli, R. M. (2024) Nanotherapy for Cancer: Seaweed-derived iron nanoparticles. *Current Science (00113891)*, **127(6)**.

19. Subhashini, G., Ruban, P. & Daniel, T. (2018) Biosynthesis and characterization of magnetic (Fe3O4) iron oxide nanoparticles from a red seaweed gracilaria edulis and its antimicrobial activity. *Int. J. Adv. Sci. Res. Manag.*, **3**, 184–189.

20. Barroga, S. Q., Perez, J. V. D. & Rodrigues, D. F. (2022) Visible Light Photocatalytic Degradation of Methylene Blue Using Polypyrrole-Coated Molybdenum-Based Magnetic Photocatalyst. In *Materials Science Forum, Trans Tech Publications Ltd.*, **1053**, 397–404.

21. Chen, T., Zhong, L., Yang, Z., Mou, Z., Liu, L., Wang, Y., Sun, J. and Lei, W. (2020) Enhanced visible-light photocatalytic activity of g-C3N4/nitrogen-doped graphene quantum dots/TiO2 ternary heterojunctions for ciprofloxacin degradation with narrow band gap and high charge carrier mobility. *Chemical Research in Chinese Universities*, **36(6)**, 1083–1090.

22. Jin, Y., Tang, W., Wang, J., Ren, F., Chen, Z., Sun, Z. & Ren, P. G. (2023) Construction of biomass derived carbon quantum dots modified TiO2 photocatalysts with superior photocatalytic activity for methylene blue degradation. *Journal of Alloys and Compounds*, **932**, 167627.

23. Tang, E. K., Partridge, G. J., Woolley, L. D., Pilmer, L. & Lim, L. Y. (2022) Effects of formulation on the palatability and efficacy of In-Feed praziquantel medications for marine finfish aquaculture. *Marine Drugs*, **20(5)**, 323.

24. Mahdavi, M., Namvar, F., Ahmad, M. B. & Mohamad, R. (2013) Green biosynthesis and characterization of magnetic iron oxide (Fe3O4) nanoparticles using seaweed (Sargassum muticum) aqueous extract. *Molecules*, **18(5)**, 5954–5964.

25. Brand-Williams, W., Cuvelier, M. E. & Berset, C. L. W. T. (1995) Use of a free radical method to evaluate antioxidant activity. *LWT-Food Science and Technology*, **28(1)**, 25–30.

26. Daneshvar, N., Salari, D. & Khataee, A. R. (2004) Photocatalytic degradation of azo dye acid red 14 in water on ZnO as an alternative catalyst to TiO2. *Journal of Photochemistry and Photobiology A: Chemistry*, **162(2-3)**, 317–322.

27. Lemine, O. M., Madkhali, N., Alshammari, M., Algessair, S., Gismelseed, A., Mir, L. E., Hjiri, M., Yousif, A. A. and El-Boubbou, K. (2021) Maghemite (γ-Fe2O3) and γ-Fe2O3-TiO2 nanoparticles for magnetic hyperthermia applications: Synthesis, characterization and heating efficiency. *Materials*, **14(19)**, 5691.

28. Li, Y. (2022) Investigation of long-term corrosion of AA2024 and AA5119 aluminum alloys under chromate coating in marine atmosphere by electrochemical impedance technology. *International Journal of Electrochemical Science*, **17(1)**, 22014.

29. Wahyuni, E. T. & Kunarti, E. S. (2022) Green methods of chemical analysis and pollutant removal. In *Green Chemistry-New Perspectives, IntechOpen*.

30. Jubb, A. M. & Allen, H. C. (2010) Vibrational spectroscopic characterization of hematite, maghemite, and magnetite thin films produced by vapor deposition. *ACS Applied Materials & Interfaces*, **2(10)**, 2804–2812.

31. Dietrich, J., Enke, A., Wilharm, N., Konieczny, R., Lotnyk, A., Anders, A. & Mayr, S. G. (2023) Energetic electron-assisted synthesis of tailored magnetite (Fe3O4) and maghemite (γ− Fe_2O_3) nanoparticles: structure and magnetic properties. *Nanomaterials*, **13(5)**, 786.

32. Moradi, M., Vasseghian, Y., Khataee, A., Harati, M. & Arfaeinia, H. (2021) Ultrasound-assisted synthesis of FeTiO3/GO nanocomposite for photocatalytic degradation of phenol under visible light irradiation. *Separation and Purification Technology*, **261**, 118274.

33. Fatima, E., Arooj, I., Shahid, H. & Aziz, A. (2024) Characterization and applications of iron oxide nanoparticles synthesized from Phyllanthus emblica fruit extract. *Plos One*, **19(9)**, e0310728.

34. Tong, C., Jiang, S., Ye, D., Li, K., Liu, J., Zeng, X., Wu, C. and Pang, J. (2023) Enhanced mechanical property and freeze-thaw stability of alkali-induced heat-set konjac glucomannan hydrogel through anchoring interface effects of carboxylated cellulose nanocrystals. *Food Hydrocolloids*, **142**, 108812.

35. Madenci, E., Özkılıç, Y. O., Aksoylu, C. & Safonov, A. (2022) The effects of eccentric web openings on the compressive performance of pultruded GFRP boxes wrapped with GFRP and CFRP sheets. *Polymers*, **14(21)**, 4567.

36. Majinyari, S., Macedo, L. J. A., Genecya, E. C. & Chavez-Baldovino, M. C. (2025) Structural elucidation of hybrid κ/ι-carrageenan using vibrational spectroscopy: Sulfate and anhydrogalactose markers in pure and nanocomposite forms. *Journal of Applied Polymer Science*, **142(3)**, e55012. https://doi.org/10.1002/app.55012.

37. Prabakaran, S., Rupesh, K. J., Keeriti, I. S., Sudalai, S., Venkatamani, G. P. & Arumugam, A. (2024) A scientometric analysis and recent advances of emerging chitosan-based biomaterials as potential catalyst for biodiesel production: A review. *Carbohydrate Polymers*, **325**, 121567.

38. Li, Y., Zheng, J., Wang, Y., Yang, H., Cao, L., Gan, S., Ma, J. and Liu, H. (2023) Immunostimulatory activity of Astragalus polysaccharides in cyclophosphamide-induced immunosuppressed mice by regulating gut microbiota. *International Journal of Biological Macromolecules*, **242**, 124789.

39. Escuadro, C. B. & Santos, G. N. C. (2024) Thermal and Mechanical Characterization of K-Carrageenan/Graphene/Bismuth Oxide Nanocomposites. *Journal of Nanotechnology*, **1**, 7114673.

40. Prasad, R. K. M., Chidananda, S. H., Shivanand, B., Basavarajappa, H. A., Shivamallu, C., Chandraiah, R. H., Dharmashekar, C. and Kollur, S. (2025) Biological, optical and electrical behaviour of k-carrageenan/PVA/TiO_2 nanocomposite film. *International Journal of Biological Macromolecules*, **319**, 145595.

41. Al-Nahdi, Z. M., Al-Alawi, A. & Al-Marhobi, I. (2019) The effect of extraction conditions on chemical and thermal characteristics of kappa-carrageenan extracted from Hypnea bryoides. *Journal of Marine Sciences*, **1**, 5183261.

42. Pereira, L., Gheda, S. F. & Ribeiro-Claro, P. J. (2013) Analysis by vibrational spectroscopy of seaweed polysaccharides with potential use in food, pharmaceutical, and cosmetic industries. *International Journal of Carbohydrate Chemistry*, **1**, 537202.

43. Mendes, M., Cotas, J., Gutiérrez, I. B., Gonçalves, A. M., Critchley, A. T., Hinaloc, L. A. R., Roleda, M. Y. and Pereira, L. (2024) Advanced extraction techniques and physicochemical properties of carrageenan from a novel Kappaphycus alvarezii cultivar. *Marine Drugs*, **22(11)**, 491.

44. Vandanjon, L., Burlot, A. S., Zamanileha, E. F., Douzenel, P., Ravelonandro, P. H., Bourgougnon, N. & Bedoux, G. (2023) The use of FTIR spectroscopy as a tool for the seasonal variation analysis and for the quality control of polysaccharides from seaweeds. *Marine Drugs*, **21(9)**, 482.

45. Firdayanti, L., Yanti, R., Rahayu, E. S. & Hidayat, C. (2023) Carrageenan extraction from red seaweed (Kappaphycopsis cottonii) using the bead mill method. *Algal Research*, **69**, 102906.

46. Coduri, M., Masala, P., Del Bianco, L., Spizzo, F., Ceresoli, D., Castellano, C., Cappelli, S., Oliva, C., Checchia, S., Allieta, M. and Szabo, D. V. (2020) Local structure and magnetism of Fe2O3 maghemite nanocrystals: The role of crystal dimension. *Nanomaterials*, **10(5)**, 867.

47. Rana, S., Shahid, S., Iqbal, M. S., Arshad, A. & Khan, D. (2024) A nanoformulation of cisplatin with arabinoxylan having enhanced activity against hepatocellular carcinoma through upregulation of apoptotic and necroptotic pathways. *Heliyon*, **10(10)**.

48. Kuo, C. W., Shen, Y. H., Hung, I. M., Wen, S. B., Lee, H. E. & Wang, M. C. (2009) Effect of Y2O3 addition on the crystal growth and sintering behavior of YSZ nanopowders prepared by a sol–gel process. *Journal of Alloys and Compounds*, **472(1-2)**, 186–193.

49. Tronc, E., Ezzir, A., Cherkaoui, R., Chanéac, C., Noguès, M., Kachkachi, H., Fiorani, D., Testa, A. M., Grenèche, J. M. and Jolivet, J. P. (2000) Surface-related properties of γ-Fe2O3 nanoparticles. *Journal of Magnetism and Magnetic Materials*, **221(1-2)**, 63–79.

50. Andronenko, S. I., Nikolaev, A. M., Suharzhevsky, S. M., Sinelnikov, A. A., Kovalenko, A. S., Ivanova, A. G. & Shilova, O. A. (2023) Phase composition and magnetic properties of nanoparticles with magnetite–maghemite structure. *Ceramics*, **6(3)**, 1623–1631.

51. Yew, Y. P., Shameli, K., Miyake, M., Kuwano, N., Ahmad Khairudin, N. B., Mohamad, S. E. & Lee, K. X. (2016) Green synthesis of magnetite (Fe3O4) nanoparticles using seaweed (Kappaphycus alvarezii) extract. *Nanoscale Research Letters*, **11(1)**, 276.

52. Sanna Angotzi, M., Musinu, A., Mameli, V., Ardu, A., Cara, C., Niznansky, D., Xin, H. L. and Cannas, C. (2017) Spinel ferrite core–shell nanostructures by a versatile solvothermal seed-mediated growth approach and study of their nanointerfaces. *ACS Nano*, **11(8)**, 7889–7900.

53. Kalsoom Khan, A., Saba, A. U., Nawazish, S., Akhtar, F., Rashid, R., Mir, S., Nasir, B., Iqbal, F., Afzal, S., Pervaiz, F. and Murtaza, G. (2017) Carrageenan based bionanocomposites as drug delivery tool with special emphasis on the influence of ferromagnetic nanoparticles. *Oxidative Medicine and Cellular Longevity*, **2017(1)**, 8158315.

54. Oya, K., Tsuru, T., Teramoto, Y. & Nishio, Y. (2013) Nanoincorporation of iron oxides into carrageenan gels and magnetometric and morphological characterizations of the composite products. *Polymer Journal*, **45(8)**, 824–833.

55. Porta-Zapata, M., Carregal-Romero, S., Saliba, J., Urkola-Arsuaga, A., Miranda Perez de Alejo, C. B., Orue, I., Martínez-Parra, L., Di Silvio, D., Descamps-Mandine, A., Daviaud, C. and Menard, M. (2025) Synthesis and Characterization of λ-Carrageenan Oligosaccharide-Based Nanoparticles: Applications in MRI and In Vivo Biodistribution Studies. *Biomacromolecules*, **26(3)**, 1948–1967.

56. Kalsoom Khan, A., Saba, A. U., Nawazish, S., Akhtar, F., Rashid, R., Mir, S., Nasir, B., Iqbal, F., Afzal, S., Pervaiz, F. and Murtaza, G. (2017) Carrageenan based bionanocomposites as drug delivery tool with special emphasis on the influence of ferromagnetic nanoparticles. *Oxidative Medicine and Cellular Longevity*, **1**, 8158315.

57. Pacheco-Quito, E. M., Ruiz-Caro, R. & Veiga, M. D. (2020) Carrageenan: drug delivery systems and other biomedical applications. *Marine Drugs*, **18(11)**, 583.

58. Necas, J. & Bartosikova, L. (2013) Carrageenan: a review. *Veterinarni Medicina*, **58(4)**, 187–205.

59. Świętek, M., Lu, Y. C., Konefał, R., Ferreira, L. P., Cruz, M. M., Ma, Y. H. & Horák, D. (2019) Scavenging of reactive oxygen species by phenolic compound-modified maghemite nanoparticles. *Beilstein Journal of Nanotechnology*, **10(1)**, 1073–1088.

60. Shah, S. T., Chowdhury, Z. Z., Johan, M. R. B., Badruddin, I. A., Khaleed, H. M. T., Kamangar, S. & Alrobei, H. (2022) Surface functionalization of magnetite nanoparticles with multipotent antioxidant as potential magnetic nanoantioxidants and antimicrobial agents. *Molecules*, **27(3)**, 789.

61. Nughwal, A., Bharti, R., Thakur, A., Verma, M., Sharma, R. & Pandey, A. (2025) Green synthesis of iron oxide nanoparticles from Mexican prickly poppy (Argemone mexicana): assessing anti-oxidant activity for potential therapeutic use. *RSC Advances*, **15(13)**, 10287–10297.

62. Shanmugam, R., Tharani, M., Abullais, S. S., Patil, S. R. & Karobari, M. I. (2024) Black seed assisted synthesis, characterization, free radical scavenging, antimicrobial and anti-inflammatory activity of iron oxide nanoparticles. *BMC Complementary Medicine and Therapies*, **24(1)**, 241.

63. Kumar, S., Ahlawat, R. & Rani, G. (2024) Anti-oxidant and photo-catalytic activity of diamond-shaped iron-based metal-organic framework. *Inorganic Chemistry Communications*, **167**, 112661.

64. Abdullah, J. A. A., Jiménez-Rosado, M., Perez-Puyana, V., Guerrero, A. & Romero, A. (2022) Green synthesis of FexOy nanoparticles with potential antioxidant properties. *Nanomaterials*, **12(14)**, 2449.

65. Ezzine, S., Ferjani, H., Ogunjinmi, O. E. & Onwudiwe, D. C. (2025) Hematite nanoparticles synthesized by green route: characterization, anticancer and antioxidant activities. *Inorganics*, **13(5)**, 167.

66. Hoang, N. T., Mwazighe, F. M. & Le, P. C. (2023) Kinetic study on the degradation of organic pollutants in UV/persulfate and in other advanced oxidation processes: Role of radicals and improvement of the degradation rates. *Journal of Environmental Chemical Engineering*, **11(5)**, 110456.

67. Liu, L., Cui, Z., Feng, B., Sui, M., Huang, H. & Wu, Z. (2024) Synthesis of Fe_2O_3/TiO_2 photocatalytic composites for methylene blue degradation as a novel strategy for high-value utilisation of iron scales. *Materials*, **17(18)**, 4546.

68. Halfadji, A., Chougui, A., Djeradi, R., Ouabad, F. Z., Aoudia, H. & Rajendrachari, S. (2023) TiO2-decorated by nano-γ-Fe_2O_3 as a catalyst for efficient photocatalytic degradation of orange G dye under eco-friendly white LED irradiation. *ACS Omega*, **8(42)**, 39907–39916.

69. Avilés-Monreal, R., Borbón-Nuñez, H. A., Farías, M. H. & Castillón-Barraza, F. (2023) Photocatalytic activity of Fe_3O_4–Fe_2O_3 particles supported on mordenite under visible light exposure for methylene blue degradation. *SN Applied Sciences*, **5(12)**, 389.

70. Jadhav, V., Dhanwate, Y., Raut, P., Shinde, S., Sawant, R. & Bhagare, A. (2025) Efficient photocatalytic methylene blue dye degradation from green-synthesized silver-doped iron oxide (Ag@ Fe_2O_3) nanostructures. *Discover Nano*, **20(1)**, 66.

71. Caf, F. (2023) Biogenic synthesis of iron oxide nanoparticle using Padina Pavonica extract: application for photocatalytic degradation of congo red dye, neurotoxicity and antioxidant activity. *Turkish Journal of Fisheries and Aquatic Sciences*, **23(2)**. TRJFAS21398.